RSC Applied Interfaces

ROYAL SOCIETY OF CHEMISTRY

PAPER

View Article Online
View Journal

Cite this: DOI: 10.1039/d5lf00384a

Self-assembled monolayer modified nickel oxide surface for air-processed blue perovskite light-emitting diodes

Jiandong Wu,[a] Yujie Wang,[a] Fankai Lin,[a] Chaoran Ni,[a] Shuhao Xiong,[a] Miao Zhang,[b] Hongyue Wang *[a] and Hongqiang Wang *[a]

Received 9th December 2025,
Accepted 15th March 2026

DOI: 10.1039/d5lf00384a

rsc.li/RSCApplInter

Ambient-air fabrication of blue perovskite light-emitting diodes (PeLEDs) presents a significant pathway toward accelerating the commercialization of perovskite displays. However, a primary challenge still remains in deteriorating perovskite crystallization caused by absorption of moisture on the substrate surface. Herein, we engineered a novel composite interface comprising an inorganic transport layer and an ultra-thin self-assembled monolayer (SAM) to significantly enhance the crystallization quality of air-processed blue perovskites. The molecule of (2-(3,6-dibromo-9*H*-carbazol-9-yl)ethyl) phosphonic acid (Br-2PACz) features a hydrophobic carbazole headgroup and a strongly anchoring phosphonic acid (P–OH) tail group. The tail group establishes robust covalent P–O–Ni bonding with NiO_x nanoparticles, which effectively passivates the surface defects on the NiO_x surface and concurrently creates an enhanced interfacial dipole moment, thereby facilitating superior hole injection. Simultaneously, the peripheral carbazole headgroup enhances interfacial hydrophobicity of the NiO_x layer, thereby optimizing the crystallization of perovskites in ambient air. Ultimately, the air-processed blue perovskite films on the Br-2PACz-modified layer exhibit suppressed defect densities and enhanced photoluminescence quantum yield (PLQY), leading to a substantial improvement in the external quantum efficiency (EQE) for blue PeLEDs from 0.73% to 3.32% in ambient air ($T \approx 21$ °C, RH ≈ 20%).

Introduction

Solution-processed metal halide perovskites (MHPs) have attracted significant attention in the field of next-generation optoelectronics, owing to their high color purity, tunable bandgaps and high photoluminescence quantum yield (PLQY).[1–3] The state-of-the-art perovskite light-emitting diodes (PeLEDs) have achieved landmark efficiencies, with record external quantum efficiencies (EQEs) now surpassing 30% for green and red PeLEDs,[4,5] as well as reaching above 26% for blue PeLEDs.[6] However, the fabrication of these high-performance devices is currently confined to inert-atmosphere gloveboxes with nitrogen environments, which significantly hinders their commercialization.[7] The recent development of ambient air-processing techniques for perovskite film fabrication has demonstrated significant potential for low-cost and scalable manufacturing of PeLEDs.[8,9] However, there is still a major challenge that moisture and oxygen can disrupt the crystallization process of perovskites, resulting in poor film optical properties.[10–12] Particularly for high moisture-sensitivity blue perovskites, ambient humidity substantially degrades film quality and decreases photoluminescence quantum yield (PLQY), constraining the record EQE of air-processed blue PeLEDs to only 5.89%.[13,14] Therefore, developing novel strategies that enable efficient and reproducible blue device fabrication under ambient air conditions is crucial for the future commercialization of PeLEDs.

Many efforts have been devoted to enhancing the crystallization quality of perovskites under ambient air conditions. For example, typical weakly polar antisolvents such as diethyl ether[13] and *n*-hexane[15] effectively narrow the crystallization window of perovskites in ambient air, thereby enhancing the crystallinity and luminescence properties of the blue perovskite films. Also, a series of additive strategies have been developed to mitigate the detrimental effects of moisture by chemical elimination of residual water from perovskite precursors[9,16] and strengthening the ionic interaction among perovskite crystals to improve their environmental stability.[17] However, these strategies improved the humidity stability of the perovskite active layer,

[a] *State Key Laboratory of Solidification Processing, Center for Nano Energy Materials, School of Materials Science and Engineering, Northwestern Polytechnical University and Shaanxi Joint Laboratory of Graphene, Xi'an, 710072, China. E-mail: hongyue.wang@nwpu.edu.cn, hongqiang.wang@nwpu.edu.cn*
[b] *Materials Institute of Atomic and Molecular Science, School of Physics & Information Science, Shaanxi University of Science and Technology, Xi'an 710021, China*

simultaneously deteriorating interfacial properties under moisture attack, which remain the key constraint for high-performance air-processed PeLEDs.[18] Particularly at buried interfaces, studies have confirmed that even trace amounts of moisture adsorbed on the substrate hole transport layers (HTLs) can severely disrupt the nucleation and crystallization processes of perovskites, ultimately leading to spectral instability and compromised luminescence performance of the perovskite films.[19,20] Inorganic nickel oxide (NiO_x) has recently emerged as a preferred hole-transport material for air-processed PeLEDs due to its weak water-absorption nature.[21] However, pristine NiO_x nanoparticles often suffer from a high density of defect states (*e.g.*, Ni^{3+} species and oxygen vacancies) and an unideal band structure, which can cause severe non-radiative recombination and create an energy barrier for hole injection.[22] Moreover, these defects also function as primary sites for moisture attack under ambient conditions, which markedly accelerates the hydrolytic degradation of prepared perovskite films.[23] Therefore, an ideal interfacial modifier is thus urgently needed to resolve the dual challenges in NiO_x transport layers, requiring both enhanced hydrophobicity to enable moisture-resistant surfaces for perovskite crystallization in ambient air and optimized energy level alignment to promote hole injection.

Here, we propose and validated a strategy that an ultra-thin modification layer of a self-assembled monolayer (SAM) addresses the dual-challenges of moisture adsorption and energy level mismatch for the air-served NiO_x layer. The molecule of (2-(3,6-dibromo-9*H*-carbazol-9-yl)ethyl) phosphonic acid (Br-2PACz) integrates a hydrophobic carbazole headgroup and a strong phosphonic acid (P–OH) anchoring group.[24] The P–OH groups establish a strong covalent P–O–Ni bond with the NiO_x substrate, efficiently

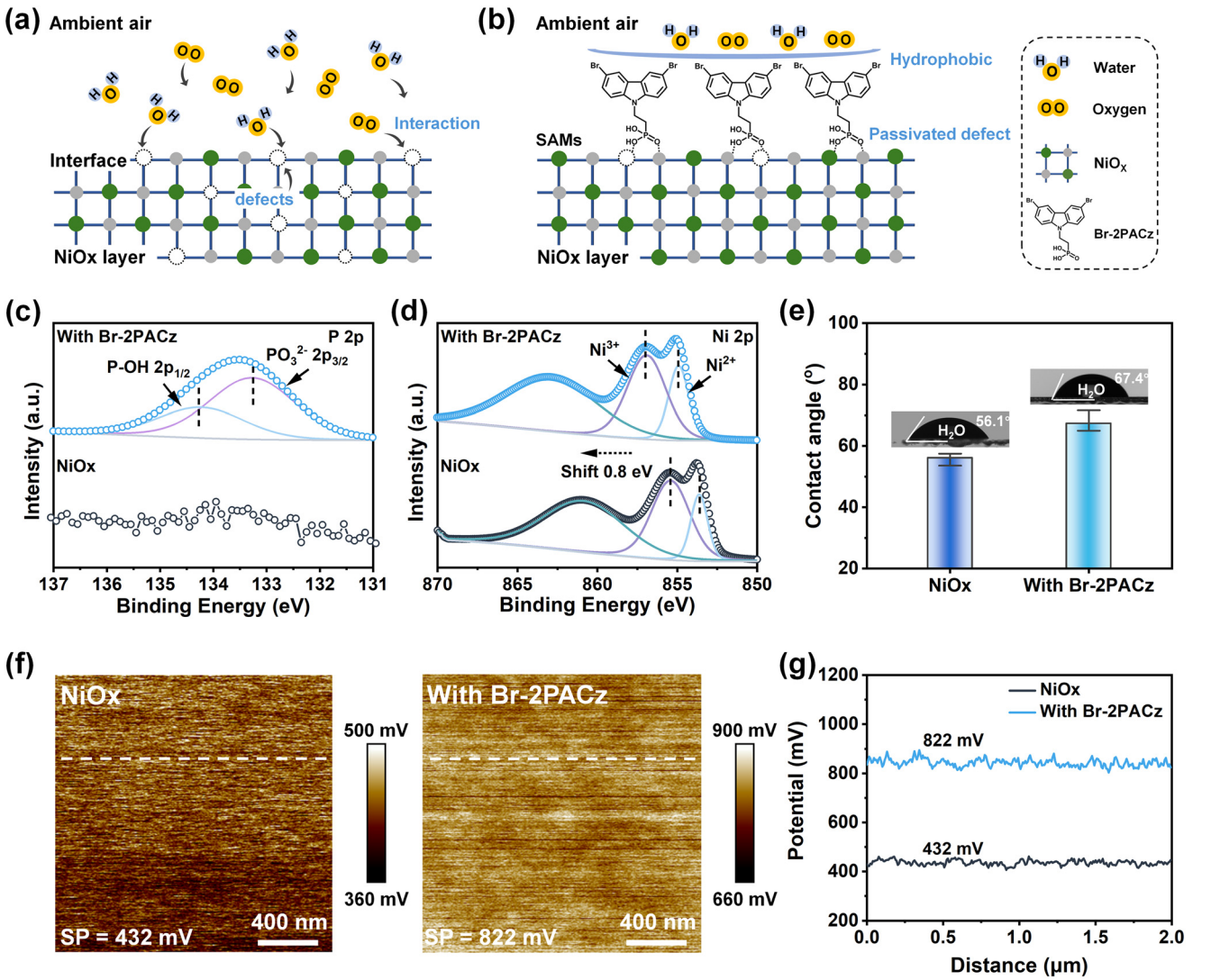

Fig. 1 (a) Schematic illustration of the interactions of moisture and oxygen with (a) the NiO_x surface and (b) the Br-2PACz-modified NiO_x surface under ambient air conditions. High-resolution XPS spectra of (c) P 2p and (d) Ni 2p of the prepared substrates. (e) The statistical water contact angles of NiO_x and Br-2PACz modified films. (f) KPFM images of the NiO_x and Br-2PACz modified films. (g) The extracted CPD changes of NiO_x and Br-2PACz modified films (along the white line in Fig. 1f).

passivating surface defects of the NiO_x layer and increasing the surface potential for enhanced hole injection. Simultaneously, the peripheral carbazole groups enhance interfacial hydrophobicity, thereby optimizing the crystallization process of perovskites in ambient air. Capitalizing on this dual advancement, Br-2PACz-modified HTLs yield air-processed blue perovskite films with suppressed trap states and enhanced PLQY (from 16.8% to 31.0%), ultimately boosting the EQE of air-processed blue PeLEDs from 0.73% to 3.32% ($T \approx 21$ °C, RH ≈ 20%). Meanwhile, when the emission area of PeLEDs is scaled up to 1.0 cm × 1.0 cm, they still maintained an EQE of 1.83%.

Results and discussion

The hole transport layers (HTLs) of Br-2PACz-modified NiO_x were fabricated *via* spin-coating (see details in the SI). The presence of Br-2PACz simultaneously passivates the defects and improves the hydrophobicity of the NiO_x surface (Fig. 1a and b). We conducted X-ray photoelectron spectroscopy (XPS) characterization to confirm the interaction between Br-2PACz molecules and NiO_x. As shown in Fig. 1c, the characteristic peaks observed at 134.2 eV and 133.2 eV correspond to P $2p_{1/2}$ and P $2p_{3/2}$ respectively, which are associated with –P–OH and $-PO_3^{2-}$ functional groups. The electronegative $-PO_3^{2-}$ group in Br-PACz provides a potential site for chemical interaction with NiO_x. Meanwhile, the Ni 2p signal in the Br-2PACz modified film shifts by approximately 0.8 eV to a lower binding energy (Fig. 1d) and exhibits a reduced Ni^{3+} content compared with that of NiO_x film (Table S1), which indicates the formation of a chemical bond between Br-2PACz and NiO_x *via* P–O–Ni. This strong anchoring between Br-2PACz and NiO_x is further confirmed by the presence of the P–O–Ni signal at 532.2 eV in the O 1s spectrum (Fig. S1). To evaluate the water resistance of these substrates, we measured the contact angles of water droplets on NiO_x and Br-2PACz-modified film, respectively. As shown in Fig. 1e and. S2, the Br-2PACz-modified film exhibits an increased contact angle, rising from 56.1° to 67.4° compared to the NiO_x film. The enhanced contact angle effectively prevents the adsorption of atmospheric moisture on the surface (Fig. S3), thereby promoting more uniform nucleation and optimizing the crystal growth process of the perovskite. Additionally, the enhanced interfacial hydrophobicity effectively accelerates the perovskite crystallization rate, thereby shortening the window of exposure to ambient moisture during film formation, which contributes to the formation of high-quality, uniformly blue perovskite films under ambient air conditions (Note S1). Atomic force microscopy (AFM) and Kelvin probe force microscopy (KPFM) were employed to characterize the surface roughness and surface potential of these films. As shown in Fig. S4, the Br-2PACz-modified film exhibits a lower surface roughness of 3.46 nm compared to the NiO_x film (4.17 nm), indicating that Br-2PACz makes the NiO_x surface flatter and helps reduce surface defects. By leveraging the pronounced conjugation group of carbazole, the Br-2PACz-modified film exhibits a significantly elevated average surface contact potential difference (CPD = 822 mV) compared with that of NiO_x film (CPD = 432 mV), as shown in Fig. 1f and g. The increased surface potential effectively reduces the carrier transport barrier at the interface, thereby enhancing hole injection efficiency from the HTLs to the perovskite film.

The blue quasi-2D perovskite films were spin-coated onto the substrates and annealed under ambient conditions ($T \approx 21$ °C, RH ≈ 20%). As shown in Fig. 2a, these perovskite films display a prominent primary PL emission peak at 480 nm, along with inapparent shoulder peaks at 435 nm and 465 nm, which are attributed to the PL from low-dimensional phases.[25] Notably, a significant enhancement in the PL intensity is observed in the film deposited on the Br-2PACz-modified NiO_x substrate, indicating a considerable improvement in the radiative recombination efficiency of the perovskite. We employed UV-vis absorption spectroscopy to characterize the phase distribution of these quasi-2D perovskite films. As shown in Fig. 2b, the absorption features at 432 nm and 462 nm can be assigned to the $n = 2$ and $n = 3$ phases, respectively. On the Br-2PACz-modified NiO_x substrate, the perovskite film exhibits an increased proportion of the $n = 3$ phase. This effectively alleviates the undesirable electron–phonon coupling induced by the quantum confinement of low-dimensional phases and promotes efficient charge carrier transport within the quasi-2D perovskite film.[26] Consequently, the perovskite film on the Br-2PACz-modified NiO_x shows a significant increase in PL quantum yield (PLQY) to 29.30%, up from 17.28% on the NiO_x substrate (Fig. 2c and S5). Atomic force microscopy (AFM) was used to characterize the surface morphology of these perovskite films. As shown in Fig. 2d, the film on the Br-2PACz-modified NiO_x substrate exhibits a much smoother surface with a reduced roughness of 1.20 nm, compared to the 6.53 nm roughness of the film on the NiO_x substrate. This enhanced film uniformity is attributed to the substantial reduction of perovskite component segregation on Br-2PACz-modified substrates (Fig. S6), thus effectively passivating crystalline defects in the perovskite film.

We performed time-resolved photoluminescence (TRPL) measurement to characterize the carrier recombination dynamics of these perovskite films (Fig. 2e), and the statistical result is shown in Table S2. The film on the Br-2PACz-modified substrate shows an enhanced average decay time (τ_{avg}) of 10.85 ns, which represents a two-fold increase compared to that of the film on NiO_x (τ_{avg} = 5.40 ns). Notably, on the Br-2PACz-modified NiO_x substrate, the increased fraction of τ_2 (7.75 ns) in the perovskite film further confirms the reduction of trap-assisted recombination, thereby enhancing the luminescence performance of the perovskite film.[27] To further investigates the carrier dynamics and trap density of the perovskite films, space-charge limited current (SCLC) measurements were conducted by fabricating hole-only devices. The dark current density–voltage (J–V) curves are presented in Fig. 2f. The J–V curve in the SCLC model is typically divided into three distinct regions: the ohmic region at low bias, the trap-filling limit (TFL) region, and the trap-

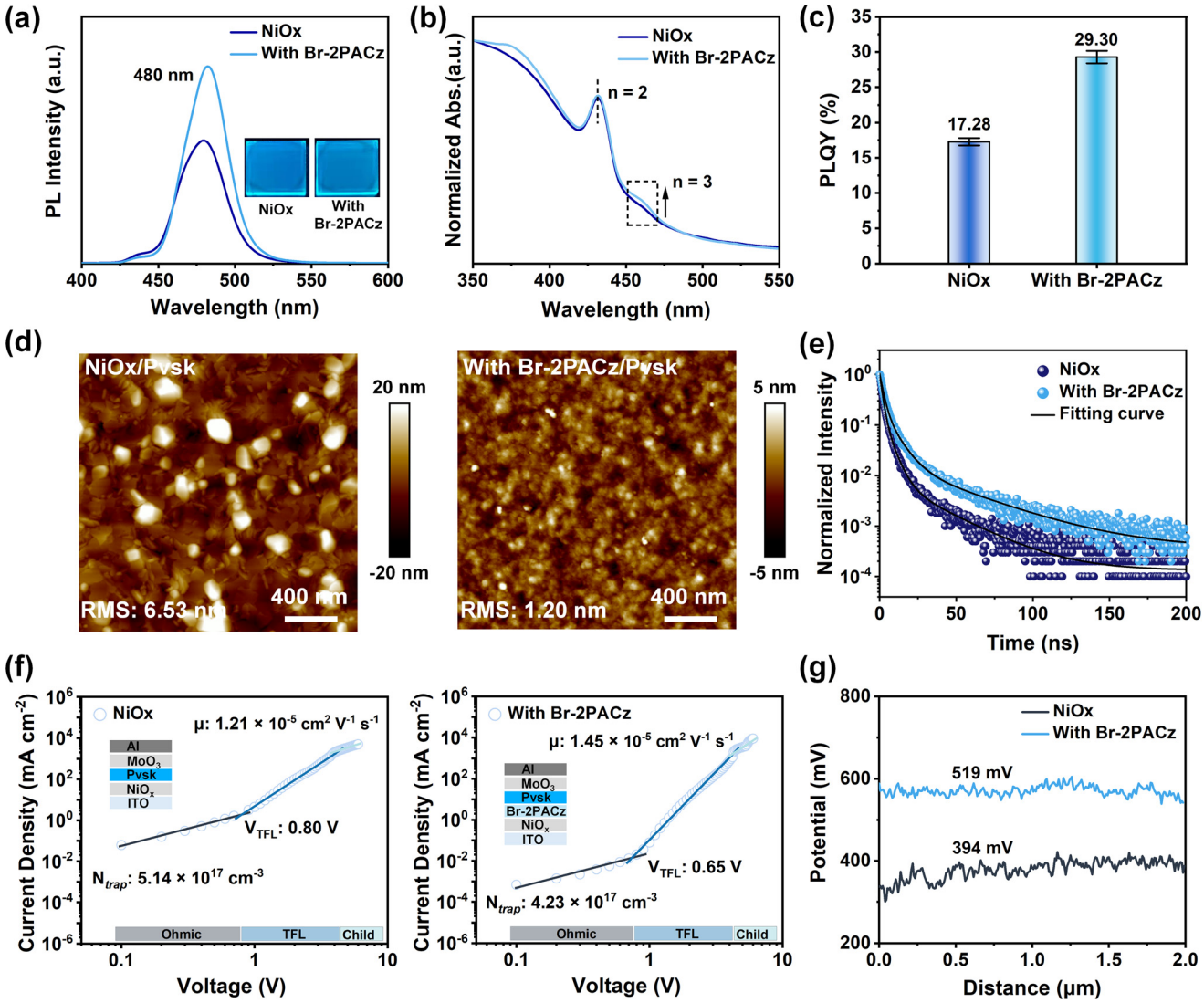

Fig. 2 (a) The PL spectra (inset shows the photos of prepared perovskite films), (b) UV-vis spectra and (c) the statistical PLQY of air-processed perovskite films on both substrates. (d) AFM images and (e) TRPL spectra of these air-processed perovskite films. (f) Space charge-limited current (SCLC) measurements based on different substrates (inset shows the device structure with an active area of 0.04 cm^2). (g) KPFM images of the perovskite films on NiO_x and Br-2PACz modified films.

free Child's region at high bias.[28] The trap-filling limited voltage (V_{TFL}) can be extracted from the turning point between the ohmic and TFL regions, which is used to calculate the trap density (N_t) using the following equation:

$$N_t = \frac{2\varepsilon_0\varepsilon_r V_{TFL}}{qL^2}$$

Furthermore, the carrier mobility (μ) can be calculated by fitting the Child's region at high voltage using the Mott–Gurney Law:[29]

$$J = \frac{9}{8}\mu\varepsilon_0\varepsilon_r\frac{V^2}{L^3}$$

where J is the current density, μ is the carrier mobility, V is the applied voltage, ε_0 is the vacuum permittivity, ε_r is the relative dielectric constant ($\varepsilon_r \approx 14.52$), V_{TFL} is the trap-filled limit voltage, q is the elemental charge ($q = 1.60217 \times 10^{-19}$) and L is the thickness of perovskite films ($L \approx 50$ nm). As shown in Fig. 2f, the V_{TFL} for the device incorporated Br-2PACz is significantly reduced to 0.66 V, compared to 0.80 V for the control device. The calculated trap density (N_t) is also reduced from 5.14×10^{17} cm^{-3} (NiO_x) to 4.23×10^{17} cm^{-3} (with Br-2PACz). Meanwhile, the hole mobility (μ) increased from 1.21×10^{-5} cm^2 V^{-1} s^{-1} (NiO_x) to 1.45×10^{-5} cm^2 V^{-1} s^{-1} (with Br-2PACz). This SCLC analysis provides strong support that the Br-2PACz modification not only effectively passivates the trap states within the perovskite film but also promotes the efficiency of hole transport. Kelvin probe force microscopy (KPFM) was employed to characterize the surface potential distribution of these perovskite films. As shown in Fig. 2g and S7, the Br-2PACz-modified NiO_x substrate yields a perovskite film with a contact potential difference (CPD) of

519 mV, which is higher than that of the perovskite film on NiO_x (394 mV). This enhanced surface potential further confirms improved charge carrier transport capability within the perovskite layer,[30] which is consistent with the results of enhanced PLQY and a prolonged carrier lifetime.

The nucleation and crystallization processes of blue quasi-2D perovskites on substrates with and without Br-2PACz modification were further systematically investigated. To verify potential pre-nucleation interactions, perovskite components ($PbBr_2$ and CsBr) were thoroughly blended with respective hole transport materials (NiO_x and Br-2PACz). As shown in Fig. 3a and b, when mixed with NiO_x, the characteristic XPS signal of Pb 4f and Cs 3d remained nearly identical to those of the pure $PbBr_2$ and CsBr references, indicating the absence of chemical interaction. In contrast, introduction of Br-2PACz into the mixture induced clear shifts for both peaks toward lower binding energies. Meanwhile, FT-IR analysis reveals that the C–Br vibration peak of the Br-2PACz exhibits a significant redshift from 733.31 cm^{-1} to 732.34 cm^{-1} upon mixing with the perovskite components (Fig. S8).[31] These results confirm the pre-interaction between Br-2PACz and the perovskite components, which helps establish abundant nucleation sites on the buried interface that direct and facilitate perovskite crystallization on the substrate.[32]

We continuously monitored the PL intensity evolution during the spin-coating and annealing stages of the perovskite film by using a home-made *in situ* PL spectroscopy

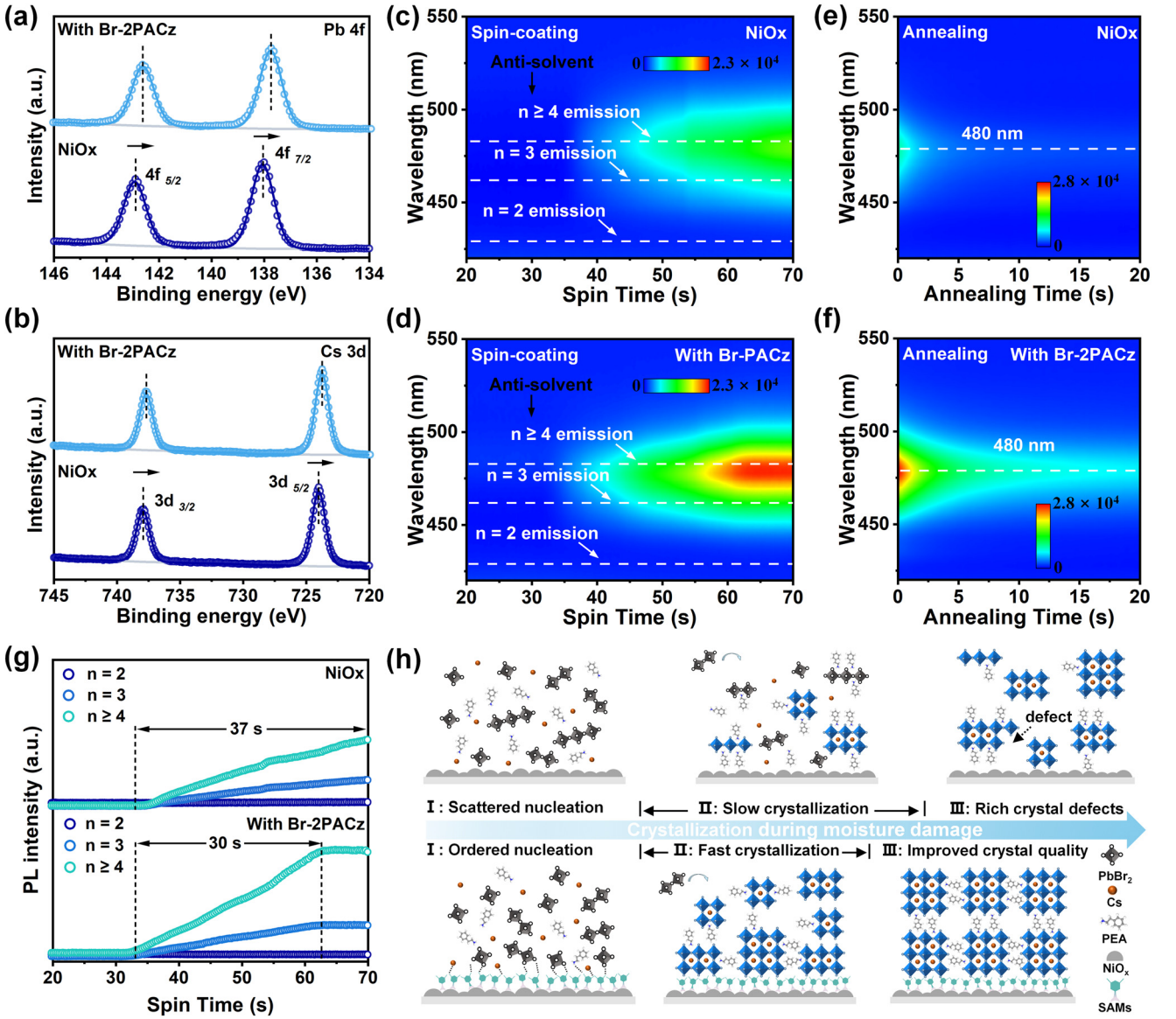

Fig. 3 XPS spectra of (a) Pb 4f and (b) Cs 3d for the mixture with NiO_x, Br-2PACz and perovskite components of CsBr and $PbBr_2$. *In situ* PL spectra of perovskite fabrication during (c and d) spin-coating and (e and f) annealing process on NiO_x and Br-2PACz modified films, respectively. (g) The extracted evolution of PL intensity from the *in situ* PL spectra in spin-coating (Fig. 3c and d). (h) Schematic illustration of the crystallization process of air-processed perovskites on NiO_x and Br-2PACz-modified substrates.

system, aiming to elucidate the perovskite growth dynamics on these substrates. All PL spectra were acquired under identical measurement conditions. As shown in Fig. 3c and d, perovskite films processed on Br-2PACz-modified NiO_x substrates exhibited significantly enhanced PL intensity during spin-coating, and an extended PL thermal quenching duration was observed throughout the annealing process (Fig. 3e and f), collectively indicating improved crystallinity and reduced defect density in the perovskite films. The formation of luminescent crystals determines the PL intensity, and the time required to reach the maximum intensity serves as an indicator of the crystallization rate.[33] We further investigated the growth kinetics of distinct *n*-phases by analyzing the temporal evolution of their corresponding PL intensities extracted from Fig. 3c and d during the spin-coating process, as summarized in Fig. 3g. The characteristic emission signals for $n = 2$, $n = 3$, and $n = 4$ phases in the quasi-2D perovskite were monitored at 430 nm, 465 nm, and 479 nm, respectively. On the NiO_x substrate, all *n*-phase PL intensities exhibited continuous enhancement throughout the entire spin-coating duration, indicating ongoing perovskite crystallization. In contrast, on the Br-2PACz-modified NiO_x substrate, the PL intensities of all *n*-phases reached their maximum at 62.7 s and subsequently stabilized during the remaining spin-coating time. This shortened time to reach the PL maximum demonstrates that Br-2PACz significantly accelerates the crystallization rate of all perovskite *n*-phases. X-ray diffraction (XRD) was employed to characterize these prepared films. As shown in Fig. S9, the perovskite film deposited on the Br-2PACz modified NiO_x substrate exhibits a notably higher intensity of the characteristic (200) peak, indicating the enhanced crystallinity of perovskite film.[34] Therefore, we conclude that the abundant nucleation sites provided by Br-2PACz at the interface effectively accelerate the crystallization rate of air-processed quasi-2D perovskites, which significantly shortens

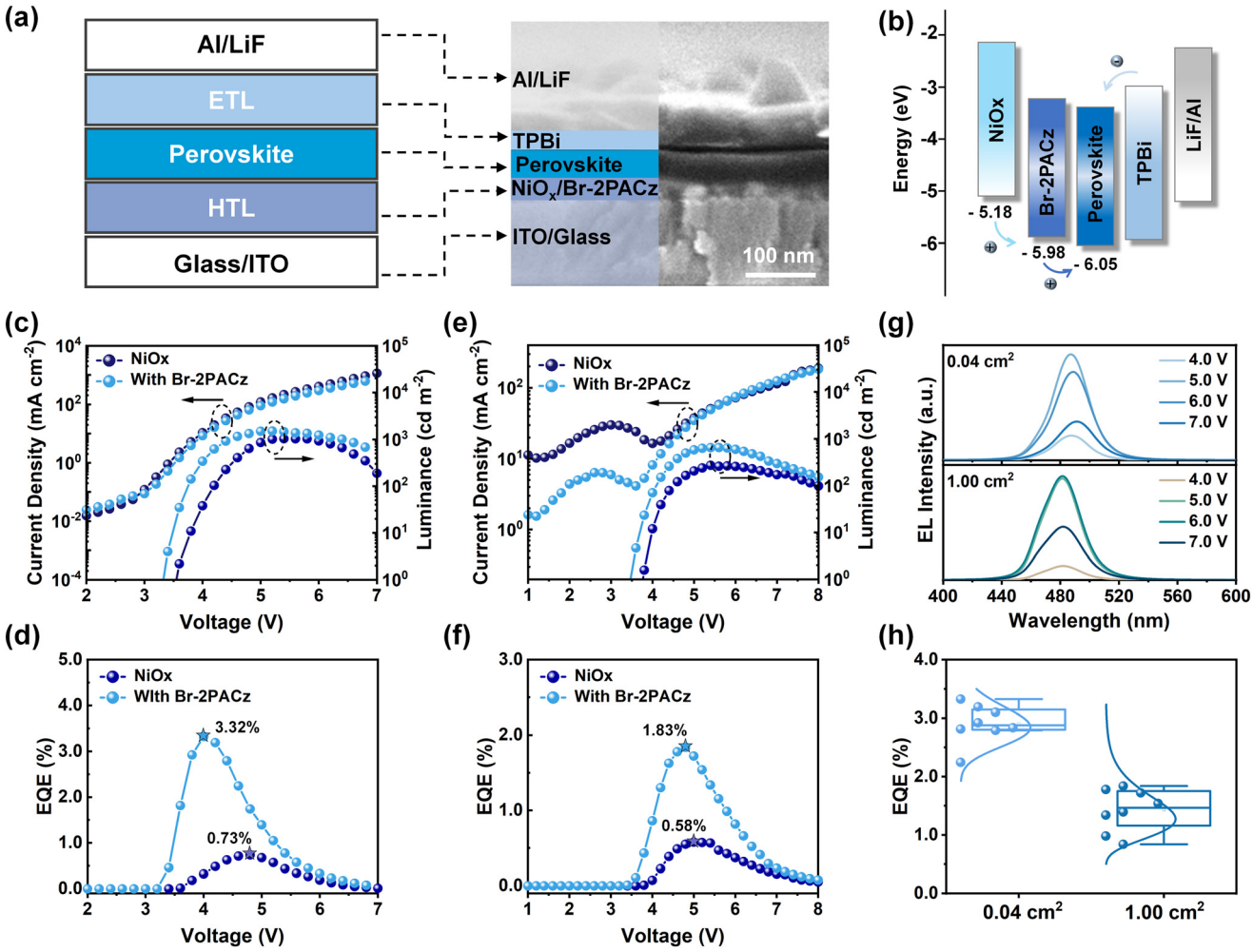

Fig. 4 (a) The PeLED structure and corresponding cross-sectional diagram of devices. (b) Schematic illustration of the hole injection between the hole transport layer and the prepared perovskite films. Current density–voltage–luminance (*J–V–L*) curves and EQE-voltage curves of air-processed PeLEDs with an emitting area of (c and d) 0.2 cm × 0.2 cm and (e and f) 1.0 cm × 1.0 cm. (g) EL spectra of the air-processed PeLEDs based on a Br-2PACz-modified substrate, measured at different voltages. (h) The statistics of EQE of these air-processed PeLEDs on the Br-2PACz-modified substrate.

the timeframe during which moisture hampers perovskite crystallization, thereby enabling the formation of uniform perovskite films with substantially improved luminescence performance (Fig. 3h).

We used the NiO_x layer, with and without Br-2PACz modification, as a hole transport substrate layer for spin-coating blue perovskite films under ambient air conditions ($T \approx 21$ °C, RH ≈ 20%), and then electron transport layers (ETLs) and aluminum (Al) were evaporated to fabricate blue PeLEDs. The device structure and SEM image in cross-sectional view of corresponding PeLEDs are shown in Fig. 4a. Ultraviolet photoelectron spectrometry (UPS) was used to assess the carrier injection barriers between these HTLs and the perovskite layer. As shown in Fig. 4b and S10, the Br-2PACz modified NiO_x layer demonstrated a deeper HOMO energy level of −5.98 eV compared to −5.18 eV for the pure NiO_x. Since the blue perovskite has a deeper valence band maximum (VBM), the deepened HOMO level of Br-2PACz modified NiO_x effectively mitigates the hole injection barrier, contributing to improve PeLED performance. Fig. 4c presents the current density–voltage–luminance (J–V–L) curves of these blue PeLEDs, where the lower current density and turn-on voltage of Br-2PACz contained PeLEDs indicates reduced interfacial defects, thereby resulting in a maximum brightness of 1512 cd m^{-2} and a peak EQE of 3.32% for the champion device; these values are higher than the control devices with a maximum brightness of 1036 cd m^{-2} and a peak EQE of 0.73% (Fig. 4d). To further evaluate the operational stability of these air-processed PeLEDs, we measured their operational half-lifetime (T_{50}) under the initial luminance of 100 cd m^2, with the constant voltage of 4 V. As shown in Fig. S11, the T_{50} of PeLEDs incorporating Br-2PACz reach to 268.2 s, which is approximately 3.17 times higher than that of the NiO_x-based device (T_{50} = 84.5 s).

Benefiting from the enhanced interfacial hydrophobicity and uniform crystallization control of the perovskite, we successfully achieved the scalable fabrication of large-area PeLEDs with a 1.0 cm × 1.0 cm emitting area under ambient air conditions. As shown in Fig. 4e, the large-area devices containing Br-2PACz exhibited an enhanced brightness of 653 cd m^{-2} and a peak EQE of 1.83% (Fig. 4f), outperforming the control devices (maximum brightness: 271 cd m^{-2}, EQE: 0.57%). Furthermore, all air-processed blue PeLEDs incorporating Br-2PACz maintained exceptional color stability, exhibiting negligible spectral shift as the operating voltage was increased from 4.0 V to 7.0 V (Fig. 4g and S12). Statistical analysis of 8 devices reveals that all air-processed PeLEDs incorporating Br-2PACz exhibited enhanced EQE compared to the control devices, alongside demonstrating excellent performance reproducibility of the Br-2PACz involved blue PeLEDs (Fig. 4h and S13).

Conclusion

In summary, the Br-2PACz modification strategy effectively mitigates the detrimental impact of interfacial moisture adsorption on the crystallization of perovskites in ambient air, owing to the enhanced defect passivation and improved hydrophobicity. Meanwhile, the Br-2PACz molecules on the NiO_x surface provide pre-nucleation coordination sites for perovskite components, promoting uniform perovskite film crystallization on the substrate. This optimized crystallization process results in air-processed blue perovskite films with suppressed defect densities and a higher PLQY. Consequently, the EQE of air-processed blue PeLEDs is significantly enhanced from 0.73% to 3.32% compared with control devices. Notably, the emission area of the PeLEDs can be scaled up to 1.0 cm × 1.0 cm while maintaining an EQE of 1.83%. This study offers a novel interfacial design strategy for the ambient-air fabrication of perovskite optoelectronic devices, thereby promotes the commercialization of perovskite-based displays.

Conflicts of interest

The authors declare no conflict of interest.

Data availability

The authors confirm that all data supporting the findings of this study are contained within the article and the supplementary information (SI), and others available from the corresponding author upon reasonable request.

Supplementary information: materials and methods were detailed as supporting information. See DOI: https://doi.org/10.1039/d5lf00384a.

Acknowledgements

This work was financially supported by the National Natural Science Foundation of China (22372132), thw National Key R&D Program of China (2023YFE0206300) and the Fundamental Research Funds for the Central Universities (G2025KY06205). We would like to thank the Analytical & Testing Center of Northwestern Polytechnical University for structure and performance characterization.

References

1 Z.-K. Tan, R. S. Moghaddam, M. L. Lai, P. Docampo, R. Higler, F. Deschler, M. Price, A. Sadhanala, L. M. Pazos, D. Credgington, F. Hanusch, T. Bein, H. J. Snaith and R. H. Friend, Bright light-emitting diodes based on organometal halide perovskite, *Nat. Nanotechnol.*, 2014, **9**(9), 687–692.

2 J. Dong, B. Zhao, H. Ji, Z. Zang, L. Kong, C. Chu, D. Han, J. Wang, Y. Fu, Z.-H. Zhang, Y. Yang, L. Zhang, X. Yang and N. Wang, Multivalent-effect immobilization of reduced-dimensional perovskites for efficient and spectrally stable deep-blue light-emitting diodes, *Nat. Nanotechnol.*, 2025, **20**(4), 507–514.

3 Y. Yu, B. F. Wang, Y. Shen, Y. T. Wang, Y. H. Zhang, Y. Y. Li, Z. H. Su, L. X. Cao, S. C. Feng, Y. H. Wu, X. Y. Gao, S. Kera,

N. Ueno, J. X. Tang and Y. Q. Li, Efficient Blue Perovskite LEDs via Bottom-Up Charge Manipulation for Solution-Processed Active-Matrix Displays, *Adv. Mater.*, 2025, **37**(37), 2503234.

4 M. Li, Y. Yang, Z. Kuang, C. Hao, S. Wang, F. Lu, Z. Liu, J. Liu, L. Zeng, Y. Cai, Y. Mao, J. Guo, H. Tian, G. Xing, Y. Cao, C. Ma, N. Wang, Q. Peng, L. Zhu, W. Huang and J. Wang, Acceleration of radiative recombination for efficient perovskite LEDs, *Nature*, 2024, **630**(8017), 631–635.

5 S. Q. Sun, J. W. Tai, W. He, Y. J. Yu, Z. Q. Feng, Q. Sun, K. N. Tong, K. Shi, B. C. Liu, M. Zhu, G. Wei, J. Fan, Y. M. Xie, L. S. Liao and M. K. Fung, Enhancing Light Outcoupling Efficiency via Anisotropic Low Refractive Index Electron Transporting Materials for Efficient Perovskite Light-Emitting Diodes, *Adv. Mater.*, 2024, **36**(24), 2400421.

6 Y. Gao, Q. Cai, Y. He, D. Zhang, Q. Cao, M. Zhu, Z. Ma, B. Zhao, H. He, D. Di, Z. Ye and X. Dai, Highly efficient blue light-emitting diodes based on mixed-halide perovskites with reduced chlorine defects, *Sci. Adv.*, 2024, **10**, eado5645.

7 M. Zhang, X. Ma, J. L. Esguerra, H. Yu, O. Hjelm, J. Li and F. Gao, Towards sustainable perovskite light-emitting diodes, *Nat. Sustain.*, 2025, **8**(3), 315–324.

8 J. Cao, X. Zhang, Y. Miao, W. Li, X. Zeng, S. Yang, C. Yan, J. Lu and W. Yang, Interactions between H2O and lead halide perovskites: Recent progress and applications, *Matter*, 2024, **7**(11), 3728–3755.

9 Y. Guo, P. Yang, F. Dong, X. Zhang, Q. Zheng, Y. Jiang, H. Wang and H. Wang, Quantum-Well Encapsulation Enabling Air-Processed Quasi-2D Perovskites with Long-Term Stability for Large-Area Deep-Blue Light-Emitting Diodes, *Adv. Funct. Mater.*, 2025, e09277.

10 K. Liu, Y. Luo, Y. Jin, T. Liu, Y. Liang, L. Yang, P. Song, Z. Liu, C. Tian, L. Xie and Z. Wei, Moisture-triggered fast crystallization enables efficient and stable perovskite solar cells, *Nat. Commun.*, 2022, **13**(1), 4891.

11 J. Tang, W. Tian, C. Zhao, Q. Sun, C. Zhang, H. Cheng, Y. Shi and S. Jin, Imaging the Moisture-Induced Degradation Process of 2D Organolead Halide Perovskites, *ACS Omega*, 2022, **7**(12), 10365–10371.

12 S. He, F. Yuan, P. Zhu, X. Wang, F. Ali, S. Zhang, P. Wu, W. Deng and Z. Wu, Multifunctional synergy of polydentate ligands enables high-performance all-bromine sky-blue perovskite light-emitting diodes, *Chem. Eng. J.*, 2026, **529**, 172867.

13 Y. Liu, T. Bu, L. K. Ono, G. Tong, H. Zhang and Y. Qi, Phase Aggregation Suppression of Homogeneous Perovskites Processed in Ambient Condition toward Efficient Light-Emitting Diodes, *Adv. Funct. Mater.*, 2021, **31**(32), 2103399.

14 Y. Duan, F. E. Oropeza, X. Jin, O. Amargós-Reyes, Y. Atoini, L. M. Cavinato, G. N. Nagy, M. U. Kahaly, V. A. de la Peña O'Shea, D. Y. Wang and R. D. Costa, Holy Water: Photo-Brightening in Quasi-2D Perovskite Films under Ambient Enables Highly Performing Light-Emitting Diodes, *Adv. Funct. Mater.*, 2022, **33**(7), 2209249.

15 S. Yang, W. Bo, J. Zhou, Y. Ji, Y. Zhang, Y. Hu, W. Zhang, J. Tang, S. Li, H. Wang, Q. Wang, X. He and H. Xu, Regulating the interaction between perovskite precursor solution and antisolvent for efficient air-processed blue perovskite light-emitting diodes, *Chem. Eng. J.*, 2025, **522**, 168194.

16 H. Wang, Y. Tong, H. Qi, K. Wang, M. Fu and H. Wang, Water assisted chlorination enables ambient air fabrication of mixed halide perovskite films for blue light emitting diodes, *J. Lumin.*, 2023, **263**, 120114.

17 Y. Guo, P. Yang, F. Dong, H. Li, J. Gao, Z. Cheng, J. Wu, Y. Xu, H. Wang and H. Wang, Lattice Stabilized and Emission Tunable Pure-Bromide Quasi-2D Perovskite for Air-Processed Blue Light-Emitting Diodes, *Adv. Sci.*, 2024, **12**(5), 2414499.

18 H. Li, J. Wu, S. Hu, W. Zhang, J. Gao, Y. Guo, P. Guo, C. Liu, G. Zhao, M. Fu, H. Bian, T. Liu, H. Wang and H. Wang, Air-Processed Blue Perovskite Light-Emitting Diodes Enabled by Manipulation of Adsorbed-Moisture-Dominated Crystallization Kinetics, *Adv. Funct. Mater.*, 2023, **33**(44), 2303787.

19 W. Li, T. Li, Y. Tong, Y. Li, H. Wang, H. Qi, K. Wang and H. Wang, Reducing Nonradiative Losses of Air-Processed Perovskite Films via Interface Modification for Bright and Efficient Light Emitting Diodes, *Adv. Funct. Mater.*, 2023, **34**(7), 2311133.

20 Y. Guo, H. Li, P. Yang, J. Gao, Z. Cheng, F. Dong, J. Wu, H. Wang and H. Wang, Perfluorooctanoic acid interface modification enabling efficient true-blue perovskite light-emitting diodes and air-processing compatibility, *Chem. Eng. J.*, 2024, **490**, 151764.

21 J. Wu, H. Li, Y. Yang, Y. Chen, Z. Wang, F. Dong, X. Liu, Y. Guo, T. Yao, Y. Xu, Q. Ye, H. Wang, H. Wang and Y. Fang, Bilateral Embedded Anchoring via Tailored Polymer Brush for Large-Area Air-Processed Blue Light-Emitting Diodes, *Angew. Chem., Int. Ed.*, 2024, e202411361.

22 F. H. Isikgor, S. Zhumagali, L. V. T. Merino, M. De Bastiani, I. McCulloch and S. De Wolf, Molecular engineering of contact interfaces for high-performance perovskite solar cells, *Nat. Rev. Mater.*, 2022, **8**(2), 89–108.

23 A. Dučinskas, G. Y. Kim, D. Moia, A. Senocrate, Y.-R. Wang, M. A. Hope, A. Mishra, D. J. Kubicki, M. Siczek, W. Bury, T. Schneeberger, L. Emsley, J. V. Milić, J. Maier and M. Grätzel, Unravelling the Behavior of Dion-Jacobson Layered Hybrid Perovskites in Humid Environments, *ACS Energy Lett.*, 2020, **6**(2), 337–344.

24 S. Liu, J. Li, W. Xiao, R. Chen, Z. Sun, Y. Zhang, X. Lei, S. Hu, M. Kober-Czerny, J. Wang, F. Ren, Q. Zhou, H. Raza, Y. Gao, Y. Ji, S. Li, H. Li, L. Qiu, W. Huang, Y. Zhao, B. Xu, Z. Liu, H. J. Snaith, N.-G. Park and W. Chen, Buried interface molecular hybrid for inverted perovskite solar cells, *Nature*, 2024, **632**(8025), 536–542.

25 Z. Chu and J. You, Blue Light-Emitting Diodes Based on Pure Bromide Perovskites, *Adv. Mater.*, 2025, **37**(25), 2409718.

26 H. Li, S. Hu, H. Wang, X. Zhang, Y. Tong, H. Qi, P. Guo, G. Zhao, J. Gao, P. Liu, J. Zang, H. Hao, T. Liu, H. Bian, Y. Zhang, Y. Wei, Y. Guo, L. Zhang, Y. Fang and H. Wang, Control of n-Phase Distribution in Quasi Two-Dimensional Perovskite for Efficient Blue Light-Emitting Diodes, *ACS Appl. Mater. Interfaces*, 2023, **15**(7), 9574–9583.

27 C. Liu, Y. Liu, S. Wang, J. Liang, C. Wang, F. Yao, W. Ke, Q. Lin, T. Wang, C. Tao and G. Fang, Highly Efficient Quasi-2D Green Perovskite Light-Emitting Diodes with Bifunctional Amino Acid, *Adv. Opt. Mater.*, 2022, **10**(13), 2200276.
28 Q. Cheng, B. Wang, G. Huang, Y. Li, X. Li, J. Chen, S. Yue, K. Li, H. Zhang, Y. Zhang and H. Zhou, Impact of Strain Relaxation on 2D Ruddlesden–Popper Perovskite Solar Cells, *Angew. Chem., Int. Ed.*, 2022, **61**(36), e202208264.
29 S. Yuan, B. Han, T. Fang, Q. Shan and J. Song, Flat, Luminescent, and Defect-Less Perovskite Films on PVK for Light-Emitting Diodes with Enhanced Efficiency and Stability, *ACS Appl. Electron. Mater.*, 2020, **2**(11), 3530–3537.
30 L. Liu, Y. Yang, M. Du, Y. Cao, X. Ren, L. Zhang, H. Wang, S. Zhao, K. Wang and S. Liu, Self-Assembled Amphiphilic Monolayer for Efficient and Stable Wide-Bandgap Perovskite Solar Cells, *Adv. Energy Mater.*, 2022, **13**(4), 2202802.
31 P. A. Christy, A. M. F. Benial, A. John Peter and C. W. Lee, Structural and spectroscopic studies of bromofullerene, *J. Alloys Compd.*, 2019, **780**, 202–211.
32 Y. An, N. Zhang, Z. Zeng, Y. Cai, W. Jiang, F. Qi, L. Ke, F. R. Lin, S. W. Tsang, T. Shi, A. K. Y. Jen and H. L. Yip, Optimizing Crystallization in Wide Bandgap Mixed Halide Perovskites for High-Efficiency Solar Cells, *Adv. Mater.*, 2023, **36**(17), 2306568.
33 A. Ummadisingu and M. Grätzel, Revealing the detailed path of sequential deposition for metal halide perovskite formation, *Sci. Adv.*, 2018, **4**, e1701402.
34 S. He, F. Yuan, P. Zhu, F. Ali, H. Tang, S. Zhang, P. Wu, W. Deng, H. Dong and Z. Wu, Divergent Optoelectronic Tuning in Sky-Blue Quasi-2D Perovskites via Spacers Conjugation and Fluorination, *Adv. Funct. Mater.*, 2025, e23282.